ADVANCED MATERIALS TECHNOLOGIES
www.advmattechnol.de

The Nanosprouts Structural Inhomogeneity of Organic Semiconductors and the Optical Memory Properties

*Lizhi Yan, Deng Zou, Yuyang Yin, Yifan Guo, Ming Chen, Xing Cheng, and Paddy Kwok Leung Chan**

Structural inhomogeneities are extensively observed in organic films. Detailed understanding of the crystal lattice packing modes and orientations of these inhomogeneity structures will provide insightful views in revealing the relationship between film morphology and device performance. Herein, this study reports a characterization approach utilizing the lateral force microscopy (LFM) to directly obtain lattice structure information on a commonly used organic small molecular material, i.e., 2,9-Diphenyl-dinaphtho[2,3-*b*:2′,3′-*f*]thieno[3,2-*b*]thiophenes (DPh-DNTT) deposited by thermal evaporation. By enhancing sensitivity, the spatial resolution of the LFM approach is optimized. The crystal structure information up to sub-molecular scale can be resolved through the optimization of the LFM test, enabling precise determination of molecular arrangements. Based on the nanosprouts structural inhomogeneity, DPh-DNTT nonvolatile optical memory transistors (OMTs) are developed and the devices demonstrate intrinsic optical memory property with a long retention time of over 1×10^4 s, accompanied by a binary state current ratio greater than 10^5. Besides proposing the utilization of Kelvin probe force microscope (KPFM) and LFM to identify the charge trapping sites of the OMT, a 16 × 16 flexible active matrix OMT array is fabricated with image processing capability. The devices showcase their potential for applications in the field of machine vision.

1. Introduction

Optical memory transistors (OMTs) represent a promising avenue for the next-generation memory circuits by integrating optical memory capabilities with well-established transistor structures.[1–4] Organic OMTs, in particular, have emerged as a promising technology due to their advantages of being lightweight, cost-effective, and easily integrable into flexible and wearable applications. In recent decades, various organic OMTs have been developed and classified according to their charge trapping mechanisms, including photochromic,[5–7] functional dielectric,[8–10] floating gate,[11–13] and heterostructure configurations.[14,15] These devices have demonstrated significant advancements, such as on/off ratios up to 10^8 and charge retention with a drain current decrease of less than 0.4 order after 10^8 s.[16,17] However, the fabrication of these devices typically involves additional processes, such as blending photochromic molecules, functionalizing dielectric layers, fabricating floating gates, and forming heterostructures, which are not cost-effective for developing flexible systems. To simplify fabrication and reduce costs, OMTs with intrinsic optical memory properties confined to the semiconductors have been introduced, eliminating the need for additional processing steps.[18,19]

Salleo et al. first observed photoinduced bias-stress reversal in a transistor utilizing poly (9,9′-dioctylfluorene-co-bithiophene) (F8T2) as the active layer.[20] Further research explored various organic molecules like 4(HPBT)-benzene,[21] sexithiophene (6-T),[22] copper phthalocyanine (CuPc),[23] NDI(2OD)(4tBuPh)-DTYM2,[24] and rubrene as photoactive channels.[25] Typically, the underlying mechanism of photoactive behavior in these devices is attributed to charge trapping at the semiconductor-dielectric interface. In the state-of-the-art research on OMTs with intrinsic optical memory properties, devices based on nanosprouts structures have demonstrated superior memory performance. These include an on/off ratio exceeding 10^6, mobility high as 7.7 $cm^2 V^{-1} s^{-1}$, and retention times for more than 6 h.[18,19] Despite the correlation between the presence of nanosprouts structures and enhanced memory performance, the charge trapping mechanisms remain unclear. A comprehensive study that investigates the correlation between the lattice packing of nanosprouts structures and the memory properties of these OMTs is crucial. Such research would provide valuable insights into the underlying

L. Yan, D. Zou, Y. Yin, Y. Guo, P. K. L. Chan
Department of Mechanical Engineering
The University of Hong Kong
Pokfulam Road, Hong Kong, P. R. China
E-mail: pklc@hku.hk

D. Zou, P. K. L. Chan
Advanced Biomedical Instrumentation Centre Hong Kong Science Park
Shatin, Hong Kong, P. R. China

M. Chen, X. Cheng
Department of Materials Science and Engineering
Southern University of Science and Technology
Shenzhen 518055, P. R. China

The ORCID identification number(s) for the author(s) of this article can be found under https://doi.org/10.1002/admt.202500197

DOI: 10.1002/admt.202500197

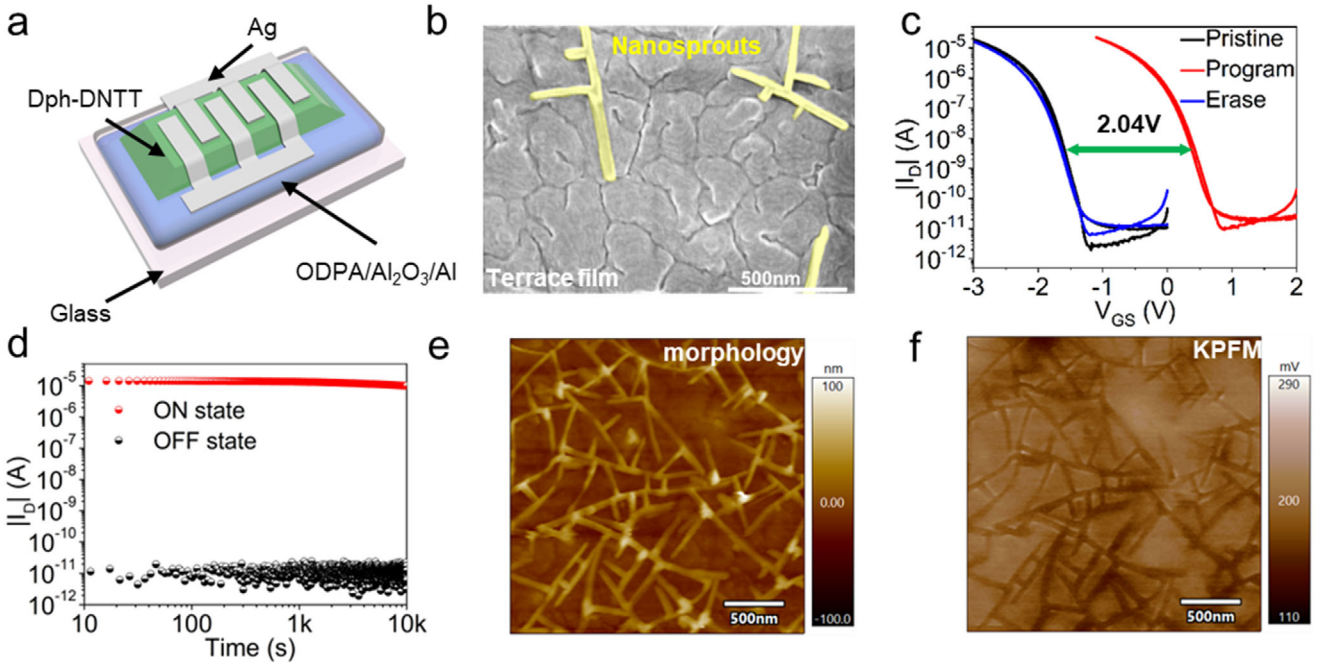

Figure 1. The optical memory properties caused by the nanosprouts structures. a) Device structure of the optical memory transistor, the DPh-DNTT film is evaporated at a substrate temperature of 100 °C. b) SEM image of the DPh-DNTT film evaporated at a substrate temperature of 100 °C, the nanosprouts structures are colored manually. c) Transfer curves of the pristine, after programing and after erasing of the optical memory transistor, V_{DS} = −3 V. d) Retention test of the optical memory transistor, current read at V_{GS} = 0 V, V_{DS} = −0.1 V. e,f) AFM topography image and the corresponding KPFM potential distribution map of the channel area of the OMT after programing.

memory mechanisms and would advance the development and application of OMTs with nanosprouts structures.

Lateral force microscopy (LFM), invented in 1987 by Mate and colleagues,[26] has played a significant role in nanomechanics research.[27–30] In addition to its contributions to this domain, LFM has demonstrated the capability for atomic resolution imaging in both contact mode and non-contact mode tests.[31–34] Its relatively minor damage on organic materials makes it a promising characterization technique for directly acquiring the molecular lattice packing information. However, current LFM imaging of lattice structures in organic films primarily focuses on the herringbone type.[35–40] While these demonstrations are important, it remains uncertain whether LFM is a viable option for routine organic lattice structures imaging, particularly given the diversity of lattice packing modes in organic films.

In this study, we developed a nonvolatile OMT based on the nanosprouts structures of DPh-DNTT film, wherein the active layer exhibits intrinsic optical memory properties. By incorporating an aluminum oxide (Al_2O_3) high-k dielectric, the OMT operates at voltages below 4 V and demonstrates promising data retention performance, maintaining a binary states current ratio exceeding 10^5 for 1×10^4 s and a predicted current ratio larger than 10^4 for 8.9×10^8 s. Subsequently, we employed LFM under ambient conditions to directly characterize the lattice structures at the grain boundaries of the DPh-DNTT films. In the film, nanosprouts structures are molecules under a "face on" packing mode with their c-axis parallel to the substrate surface, while the terrace structures are molecules standing upright on the substrate. Additionally, finer crystal packing information in nanosprouts structures can be obtained by employing probes with enhanced sensitivity. The exposed lattice plane in the nanosprouts structures is characterized as the (110) plane. To the best of our knowledge, this is the first time the exposed surface lattice packing information of this kind of film has been reported. We show that LFM imaging of sub-molecular resolution can be achieved even in ambient condition tests through autocorrelation function (ACF) filtering. Furthermore, by using high-resolution Kelvin probe force microscopy (KPFM) and LFM, the location of the charge trapping sites is concluded to be at the interface between the nanosprouts structures and the terrace structures. Beyond the working principle of the OMTs, we further demonstrate their application potential by fabricating a 16 × 16 flexible active matrix OMT array, showcasing image recognition and storage functions.

2. Results and Discussion

2.1. The Optical Memory Properties Caused by the Nanosprouts Structures

The structural inhomogeneities in organic films offer the potential of generating intriguing phenomena, for instance, optical memory phenomenon stemmed from the lattice structures mismatch. We utilized the bottom gate top contact (BGTC) transistor structure to investigate the optical memory properties caused by the nanosprouts and the schematic drawing of the OMT device structure is shown in **Figure** 1a. A false colored scanning electron microscopy (SEM) image of DPh-DNTT film is showcased in Figure 1b. The film thickness is 40 nm and is subjected to thermal evaporation at a substrate temperature of 100 °C. This

thickness is maintained throughout all subsequent sections unless otherwise specified. As shown in Figure 1b, both terrace structures, and nanosprouts structures (highlighted in yellow) can be observed, and the detailed investigations of these structures will be discussed in the following sections. The memory performance of the OMT is evaluated by the optical-electrical programing and erasing process. Under the program condition: gate-source voltage (V_{GS}) = 4 V, drain-source voltage (V_{DS}) = 0 V, and 445 nm light illumination at a power density of 20 mW cm^{-2} for 10 s, the threshold voltage (V_{TH}) value of the transfer curve shifts 2.04 V toward positive side as shown in Figure 1c. The transfer curve of the device reverses back to the pristine state with the erase condition: $V_{GS} = -4$ V, $V_{DS} = 0$ V for 10 s., i.e., 445 nm blue light and positive gate bias are used for programing, and negative gate bias with no light are used for erasing. The retention test results in Figure 1d show that after the programming process, the on/off state current ratio of the OMT can remain larger than 10^5 for longer than 1×10^4 s, and the projected time for a current ratio longer than 10^4 is 8.9×10^8 s (Figure S1, Supporting Information). The V_{TH} shift values of this OMT are adjustable and affected by factors of optical power density, programing duration, and programing gate bias value. As depicted in Figure S2 (Supporting Information), a longer programing duration, a higher optical power density, and an increased programing gate bias value result in a more rapid V_{TH} shift. On the other hand, if the positive gate bias or light illumination are applied individually during the programing process, or the light illumination is combined with negative gate bias rather than positive bias, these do not lead to a significant V_{TH} shift (Figure S3, Supporting Information). The fatigue test results for this OMT are presented in Figure S4a (Supporting Information). After 300 program-erase cycles, the OMT exhibits a slight decrease in the programming state current while maintaining a relatively stable erasing state current. By assuming an on/off ratio of 10^3 as the minimum requirement for the operation of the OMT devices, the extrapolated results in Figure S4b (Supporting Information) suggest a device lifetime of $\approx 1.1 \times 10^4$ cycles.

To elucidate the charge trapping mechanism of the optical memory phenomenon, we conducted KPFM test on the channel area of the OMT after programing. The KPFM test was first calibrated on the standard Al/Au sample, as presented in Figure S5 (Supporting Information). The morphology image and the corresponding KPFM potential map of the channel area of DPh-DNTT film after programing are presented in Figure 1e,f. Notably, the potential distribution exhibits a strong correlation with the nanosprouts structures shown in the morphology image. The potential distribution of nanosprouts structures demonstrated a lower value compared to the surrounding terrace film after programing, showcasing an average reduction of ≈15% compared to the adjacent areas along the diagonal, as demonstrated in Figure S6 (Supporting Information). This observation suggests that the work function of the nanosprouts structures tend to align more closely with the highest occupied molecular orbital (HOMO) after programing. It can be understood as during the programing process, charge accumulation occurs within or adjacent to the nanosprouts structures, which are the origins of the memory properties. We further deposited DPh-DNTT and copper hexadecafluorophthalocyanine (F_{16}CuPc) films on the OTS/SiO_2/Si structure at a substrate temperature of 100 °C and explored their memory performances, as presented in Figure S7 (Supporting Information). Generally, the DPh-DNTT film on the OTS/SiO_2/Si substrate exhibited nanosprouts structures and significant optical memory performance. In contrast, the F_{16}CuPc film on the same substrate did not display nanosprouts structures and demonstrated negligible optical memory performance.

2.2. Characterizing the Lattice Packing Modes of Inhomogeneity Structures in DPh-DNTT Film via LFM

The charge trapping sites that are crucial to the manifestation of the memory phenomenon are situated within or adjacent to the nanosprouts structures. A comprehensive understanding of the crystal lattice packing modes and orientations of these nanosprouts structures is essential for elucidating the charge trapping mechanism. LFM has been employed to directly characterize the lattice structure of these nanosprouts formations within the DPh-DNTT films. The atomic configurations of materials can be revealed through measurement of lateral forces. This concept can be comprehended through the Prandtl-Tomlinson (PT) model, which correlates the stick-slip motion with the periodic potential profile.[41–46] In the context of an LFM test, the tip exhibits a stick-slip behavior as it traverses the periodic potential defined as the summation of the Lennard-Jones potential of each surface atom interacting with the tip atom.[44,45,47] The lattice structure of DPh-DNTT crystal is exhibited in **Figure 2a**, with the dimensions along the three axes marked.[48] The schematic diagram of the LFM test is shown in Figure 2b. The cantilever of the AFM probe twists at an angle proportional to the friction force between the probe tip and the tested material. This twist angle is detected by the photodetector and generates a lateral output signal. The film morphology is characterized by the variation in friction force (Figure S8, Supporting Information). The LFM image of a selected nanosprouts-terrace interface area is displayed in Figure 2c, showing a prominent parallel structure in the nanosprouts part. The distance between two parallel structures is calculated to be 2.40 ± 0.05 nm. In the enlarged LFM image of the terrace part (Figure 2d), the lattice parameters of this herringbone structure are 0.78 ± 0.02 and 0.62 ± 0.02 nm, as shown in the inset image of Figure 2d. When compared with the lattice structure in DPh-DNTT crystal shown in Figure 2a, one can notice that the nanosprouts structures are the molecular "face on" packing mode, while the terrace structures are molecules standing upright on the substrate. The LFM test results mentioned above are conducted using a probe with a $1/hk_t$ value of 0.044 (μN)$^{-1}$, where h is tip height of the AFM probe, and k_t is torsional spring constant of the cantilever. The effects of $1/hk_t$ value on the LFM images will be further discussed.

To enhance the sensitivity of LFM measurements and reveal finer crystal packing structure within nanosprouts structures, related aspects including the origin of the LFM signal and the mechanics of the cantilever were considered. Consequently, it has been concluded that the sensitivity of LFM test increases with the increase of $1/hk_t$ value.[49,50] Detailed calculations supporting this conclusion can be found in the Supporting Information. It is important to note that an excessively small k_t value may induce a multiple-slip phenomenon,[43] thereby disrupting the accurate detection of lattice information by the LFM. To verify these

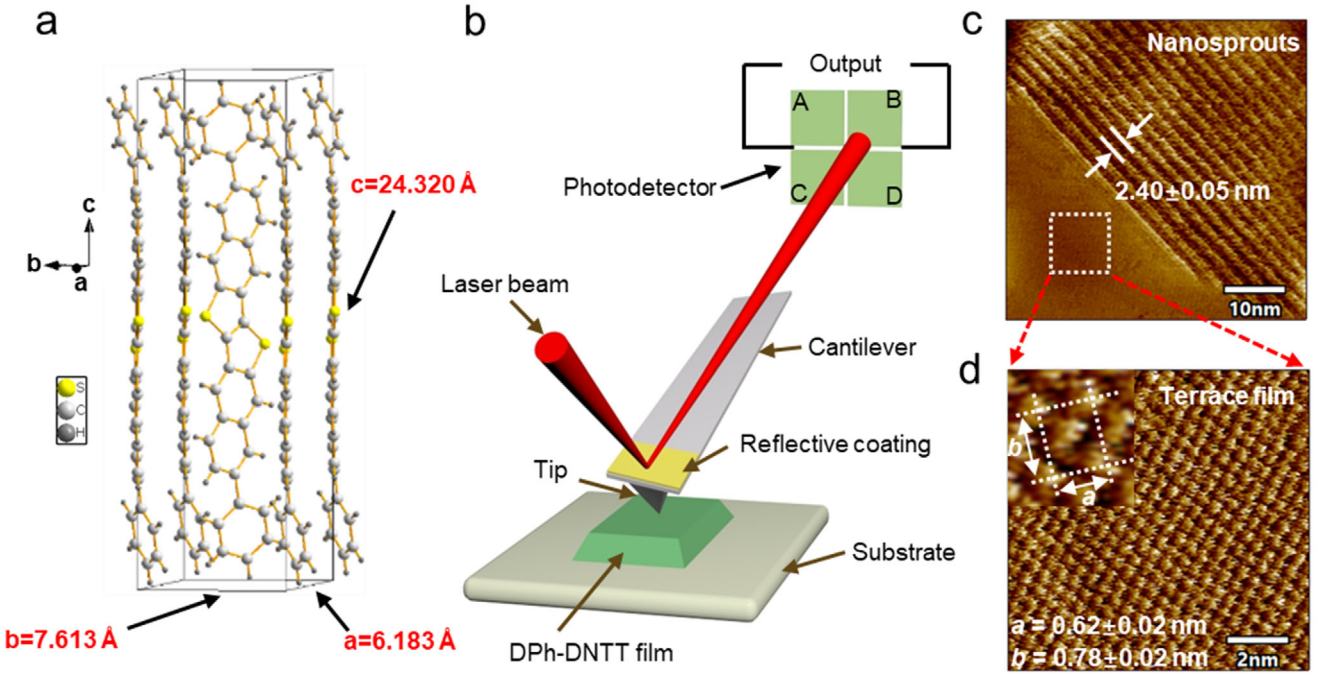

Figure 2. The lattice packing information of nanosprouts and terrace structures of DPh-DNTT film. a) Lattice structure of DPh-DNTT crystal. b) Schematic diagram of the LFM test. c) LFM image of a selected nanosprouts-terrace interface area. d) LFM image of the terrace film, the insert image in Figure 2d is the enlarged view of the herringbone structure.

assertions, we carried out LFM tests with five distinct commercially available AFM probes, each characterized by differing $1/hk_t$ and k_t values. Detailed information can be found in Figure S9 and Table S1 (Supporting Information), which successfully affirm the assertions mentioned above. An ideal AFM probe for LFM tests should possess a maximum $1/hk_t$ value while simultaneously maintaining a sufficiently large k_t value to prevent the occurrence of the multiple-slip phenomenon. An AFM probes opportunity map for LFM measurements of DPh-DNTT lattice is provided in Figure S10 (Supporting Information).

A schematic diagram of the LFM test on DPh-DNTT molecule is presented in **Figure** 3a, where the probe slides over the molecule to detect crystal packing information. The LFM image of the nanosprouts using a probe with a $1/hk_t$ value of 0.044 $(\mu N)^{-1}$ is exhibited in Figure 3b, similar to Figure 2c, it displays a single direction parallel structure, with the length between two parallel structures calculated to be 2.40 ± 0.05 nm. This corresponds to the "face on" state of the DPh-DNTT crystal packing mode. In contrast, the LFM image of the nanosprouts structure obtained using a probe with a $1/hk_t$ value of 0.056 $(\mu N)^{-1}$ reveals the presence of two distinct types of parallel structures, as shown in Figure 3c. The calculated lengths between two parallel structures are found to be 2.40 ± 0.05 nm and 0.98 ± 0.02 nm. The parallel structure with a length of 2.40 ± 0.05 nm corresponds to "face on" state of the DPh-DNTT crystal as mentioned above. The 0.98 ± 0.02 nm parallel structure exhibits a strong correlation with the diagonal of the herringbone structure, specifically the (110) plane in the DPh-DNTT lattice. The lattice arrangement of the nanosprouts, as viewed from the side and top perspectives, is depicted in Figure 3d,e, respectively. We believe that the exposure of the (110) lattice plane in the nanosprouts structures is due to the energy preferential during the organic film growth process and it is governed by the Gibbs-Curie-Wulff theorem.[51]

The LFM tests mentioned above were conducted under ambient conditions. Compared to tests conducted under ultra-high vacuum (UHV) conditions, ambient LFM measurements can potentially lead to a reduction in resolution. Factors contributing to this reduction include the capillary force from water meniscus formation, enhanced contamination effects, fluctuations in temperature and humidity, and disturbances from air movement.[52,53] Despite these negative effects, LFM results can still be enhanced to achieve sub-molecular resolution using autocorrelation function (ACF) filtering. The LFM image of the nanosprouts structure after ACF filtering is displayed in Figure 3f. Additional details regarding the principles underlying this technique, as well as the methodology, are provided in the Supporting Information. The ACF filtered image reveals periodic bright spots. The distances between successive bright spots along the longitudinal axis of DPh-DNTT molecules are 0.79 ± 0.05 nm, 0.73 ± 0.05 nm, and 0.91 ± 0.05 nm. Additionally, a distance of 0.98 ± 0.02 nm is noted between two parallel molecules, as shown in Figure S11a (Supporting Information). These lengths exhibit a strong correspondence to the lengths between the hump portions of the DPh-DNTT molecules along the lattice c-axis, as illustrated in Figure 3g and Figure S11 (Supporting Information). The units of the lengths in the schematic diagrams of Figure 3d,e,g are in sub-angstrom magnitude for practical purposes.

The cross-sectional SEM image of the evaporated DPh-DNTT film is depicted in Figure S12 (Supporting Information), revealing that the nanosprouts structure stems from the bottom part of the thin film. Figures S13 and S14 (Supporting Information)

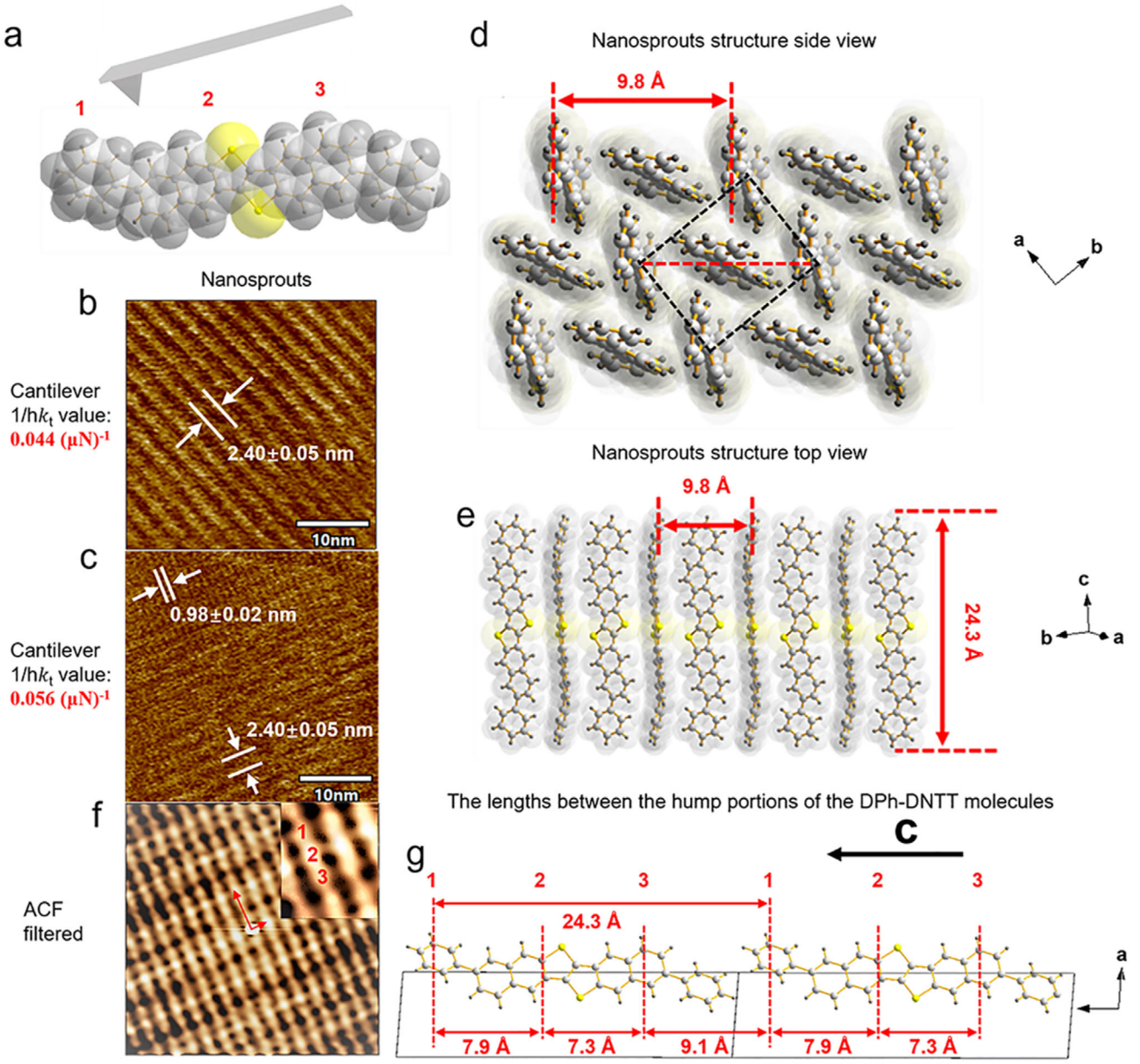

Figure 3. The methodologies for enhancing the resolution of LFM test. a) Schematic diagram of the LFM test on DPh-DNTT molecule, hump portions of DPh-DNTT molecule are marked. b,c) LFM test results of the nanosprouts structure of DPh-DNTT film of probes with $1/hk_t$ values of 0.044 $(\mu N)^{-1}$ and 0.056 $(\mu N)^{-1}$. d,e) Crystal packing mode diagrams of side view and top view of the nanosprouts structure. The black dotted line in Figure 3d depicts the herringbone structure of DPh-DNTT lattice. f) The LFM test image of nanosprouts structure after ACF filtering. The insert image is the enlarged view of the periodic bright spots. g) The lengths between hump portions of DPh-DNTT molecules along c-axis.

display the XRD results of the deposited film, indicating the presence of in-plane peaks in the out-of-plane tests. This observation aligns well with the identification of "face on " and "stand up" lattice packing modes in LFM assessments. We have further employed LFM on two commonly used organic materials, F_{16}CuPc and dinaphtho[2,3-*b*:2′,3′-*f*]thieno[3,2-*b*]thiophene (DNTT), and evaluate their lattice structures (Figure S15, Supporting Information). The comparable results with other characterization approaches suggest that the LFM has high potential for exploring the lattice configurations of polycrystalline organic semiconductors under ambient conditions.

2.3. The Charge Trapping Mechanism

Instead of using 100 °C, if the DPh-DNTT is evaporated at a substrate temperature of 25 °C under the same thickness of 40 nm, the films show no nanosprouts structures (**Figure** 4a) and

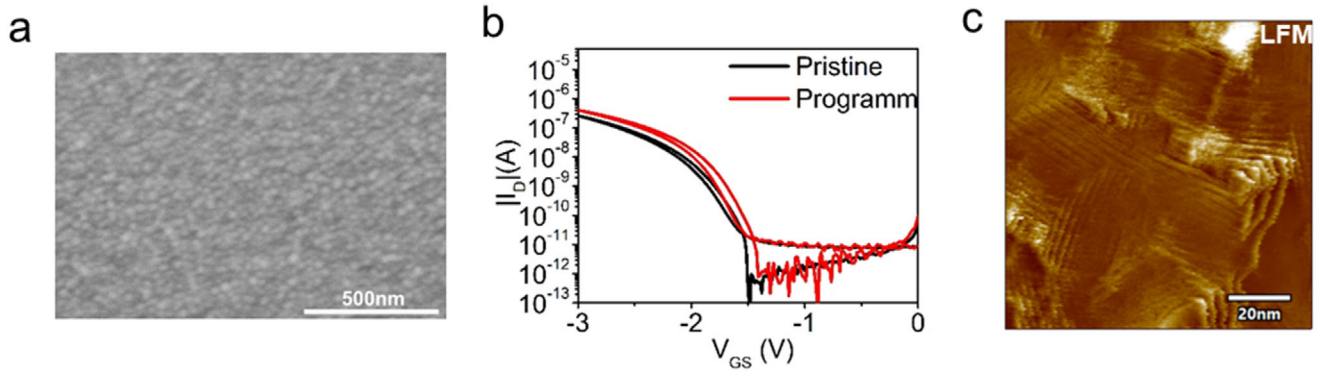

Figure 4. The nanosprouts structures-optical memory property dependent relationship. a) SEM image of the DPh-DNTT film evaporated at a substrate temperature of 25 °C. b) Transfer curves of the pristine, after programing of the transistor with DPh-DNTT film evaporated at a substrate temperature of 25 °C as active layer, $V_{DS} = -3$ V, (program condition: $V_{GS} = 4$ V, $V_{DS} = 0$ V, 445 nm optical power density of 20 mW cm^{-2}, 10 s). c) LFM image of the DPh-DNTT film evaporated at a substrate temperature of 25 °C.

negligible optical memory performance (Figure 4b). Additionally, post-annealing treatments to these films are unable to induce the nanosprouts structures and the optical memory performance, as illustrated in Figure S16 (Supporting Information). In the absence of the distinguishable nanosprouts structures, no significant optical memory performance is observed in the devices. KPFM results of transistor without nanosprouts structures and the associated optical memory phenomenon (DPh-DNTT film evaporated at a substrate temperature of 25 °C) after programing are shown in Figure S17 (Supporting Information). The KPFM potential distribution map of the channel area does not exhibit discernible charge accumulation phenomenon. We further conducted programming with a gate-source voltage of up to 8 V on transistors with DPh-DNTT semiconductors evaporated at 25 and 100 °C. The results are presented in Figure S18 (Supporting Information). An increased programming gate bias results in a more rapid V_{TH} shift (Figure S2b, Supporting Information). As expected, both types of devices exhibit a larger memory window when the programming voltage is increased to 8 V. The 25 °C transistor exhibited a memory window of 0.51 V and an on/off ratio lower than 10^3, while the 100 °C one exhibited a memory window of 4.10 V and an on/off ratio larger than 10^6. This implies that the 25 °C transistor is not suitable for effective memory device applications compared to the 100 °C one.

Given that a transistor is essentially an interface domain device, a primary research objective is to investigate whether the charge trapping sites are situated at the interface between the nanosprouts structures and the dielectric layer, or at the interface between the nanosprouts structures and terrace structures. LFM measurements are used to ascertain the lattice packing information of the film, which shows no memory effects, and to gain further insight into the locations of the charge trapping sites. The LFM test image (Figure 4c) reveals that the primary lattice packing mode in this DPh-DNTT film aligns with the "face on" mode, despite an absence of the apparent nanosprouts structures. More LFM images of this type of film can be seen in Figure S19 (Supporting Information). It is important to mention that the prominent "face on" packing mode is signature of the nanosprouts observed in the 100 °C deposited film. Since the whole film is under the "face on" lattice packing mode, the density of the "face on" state in the non-memory film (25 °C) is significantly greater than that in the memory film (100 °C). The interface area ratio between the "face on" semiconductor and the dielectric layer in the non-memory film is also larger than the film with memory. This observation contradicts to the assumption that the charge trapping sites are located at the interface between the "face on" state and the dielectric layer. Moreover, the application of post-anneal treatment to non-memory films does not induce memory performance. These results lead us to conclude that the semiconductor/dielectric interface or the bulk nanosprouts themselves are not the origin of the optical memory phenomenon. Given the actual architecture of the device and the nanosprouts structures, we believe that the charge trapping sites are positioned at the interface between the nanosprouts structures and the terrace structures.

The primary lattice packing mode in DPh-DNTT films deposited at 25 °C is characterized by a "face on" orientation. In contrast, the majority terrace structures in films deposited at 100 °C exhibit a "stand up" orientation. One of the well accepted explanations to this phenomenon is the surface mobility-diffusion distance temperature-dependent theory.[54–56] According to this theory, at lower substrate temperatures, organic molecules demonstrate limited surface mobility, restricting their ability to reconfigure easily. Consequently, the molecules align parallel to the substrate to release surface energy. Conversely, at elevated temperatures, the molecules gain increased thermal energy, which enhances their surface mobility. When the temperature is sufficiently high to provide the activation energy required for the organic molecules, a transition from a local energy minimum to a global energy minimum state occurs.[54] This transition facilitates the alignment of molecules in a "stand up" packing mode over a larger diffusion distance.

The molecular packing orientation of organic molecules is significantly influenced by material-substrate surface interactions during the growth process. In addition to the temperature effects mentioned above, we have also investigated the impact of substrate surface roughness on film morphology. The findings are presented in Figures S20-S22 (Supporting Information). Substrates with varying surface roughness were produced by adjusting the Al evaporation speed during the evaporation process. The

optical memory performance was also evaluated, as shown in Figure S22 (Supporting Information). The results indicate a positive correlation between the density of the nanosprouts structures and the substrate surface roughness values. Furthermore, the memory performance exhibits a dependency on the density of the nanosprouts structures.

The optical memory effect is correlated with the presence of these nanosprouts structures. We estimated the density of total charges trapped using the equation:

$$N_{trap} = C\Delta V_{TH}/e \quad (1)$$

where N_{trap} is the density of the total trapped charges, C is the areal capacitance of the dielectric, ΔV_{TH} is the OMT threshold volatage shift after programming, and e is the elementary charge. Under the program condition: $V_{GS} = 4$ V, $V_{DS} = 0$ V, and 445 nm light illumination at a power density of 20 mW cm^{-2} for 10 s, the V_{TH} shift value is 2.04 V. The N_{trap} is estimated to be 4.42×10^{12} cm^{-2}. We calculated the density of the nanosprouts structures via ImageJ software on SEM images shown in Figure S23 (Supporting Information); the density of the nanosprouts structures is estimated to be $\approx 8.9 \times 10^{8}$ cm^{-2}. The number of charges trapped in a single nanosprouts is estimated to be 4.96×10^{3}.

The working mechanism of the OMT can be elucidated as follows: the structural inhomogeneities between the terrace structures and the nanosprouts structures introduce crystal lattice mismatches, as previously discussed, resulting in the generation of effective charge trapping sites. The illumination involved in the programming process generates photoactivated electrons and holes. The normalized absorbance of the evaporated DPh-DNTT film is exhibited in Figure S24 (Supporting Information); note that the 445 nm light involved in the programming process is within the absorbance limit of the film. Subsequently, under the influence of positive gate bias, these photoelectrons become entrapped within the trapping sites situated at the interface between the terrace structures and the nanosprouts structures. The additional holes attracted by the trapped electrons in the channel area increase the conductivity of the transistor channel, resulting in a shift of the threshold voltage to more positive values.[57,58] An increased gate bias facilitates the accumulation of more charges in the trapping sites near the bottom channel area. During the erasing process, a negative gate bias enables the removal of the trapped electrons from the trapping sites. The extra holes induced by the trapped electrons vanish during this de-trapping process, and the device reverts to its high resistance state.[19,59] The schematic diagram of the working mechanism of the OMT is depicted in Figure S25 (Supporting Information). The dependence of the optical memory property on the nanosprouts structures in DPh-DNTT films can be attributed to the effective charge trapping sites, which arise from the crystal structure mismatch between the interface of terrace and nanosprouts configurations.[59–62]

2.4. The Demonstration of the Image Recognition and Storage OMT Array

16 × 16 flexible active matrix OMT arrays are fabricated to demonstrate the application potential of these memory transistors. The array possesses image processing capabilities, facilitated by the incorporation of both photo detection and memory functions within its design. The optical images of the fabricated OMT array are displayed in **Figure 5**a, while a zoomed-in view of the pixel area is presented in Figure 5b, and the schematic diagram of a single cell within the array is depicted in Figure 5c. The detailed fabrication process, including the photolithography and reactive ion etching processes, is provided in the Experimental Section and Figure S26 (Supporting Information). It is worth mentioning that the fabrication of an OMT array presents more challenges compared to individual devices, as a single leakage cell can cause an entire line to fail. Moreover, any inconsistencies or defects can lead to malfunction of the array, especially under image processing. This demands high homogeneity across each cell, which requires precise control in each fabrication step.

The thickness of the Al_2O_3 dielectric layers in the array is 34 nm, determined by cross-sectional scanning transmission electron microscopy (STEM) test (Figure S27, Supporting Information). The areal capacitance of the ODPA/Al_2O_3 structure in the OMT array has a mean value of 248.5 nF cm^{-2}, as depicted in Figure S28 (Supporting Information). In the fabrication process of this array, contact holes in the parylene isolation layer are created through photolithography and reactive ion etching (RIE) processes. These contact holes are situated on the gate lines, source lines, and drain lines; thus the proper functioning of the transistor cells is highly dependent on the success ratio of this procedure. The contact holes opening success ratio is measured to be 100% using a 16 × 16 electrodes crossbar structure (Figure S29, Supporting Information). The transfer curves and leakage currents for the 16 × 16 OMTs in the array are displayed in Figure S30 (Supporting Information), encompassing a total of 256 devices, as well as the statistical distribution of parameters such as mobility, V_{TH}, and on/off ratio. These 256 devices exhibit moderate performance, characterized by a mean mobility value of 2.1 cm^2 V^{-1} s^{-1}, a mean V_{TH} value of −1.0 V, a mean on/off ratio value of 9.1×10^5, and a leakage current of less than 1 nA within the scanning range of 1.5−−3 V. A customized automatic test system was developed for on-site image recognition (Figure S31, Supporting Information). The image recognition and storage functions were demonstrated using this automatic test system. The blue light (445 nm) passing through a shadow mask serves as the image input signal. The image recognition and storage capabilities of the OMT array are demonstrated in Figure 5d. The photograph on the left in Figure 5d displays the pattern of the input optical signal, while the right current map exhibits a pattern of the capital letter "H". This pattern, composed of 256 pixels, was captured after programming and turning off the light. The integration of image processing within the array itself has the potential to enhance the speed and efficiency of image processing systems, as it eliminates the necessity for external processing. The current "1T" array design exhibits cross-talk problems, which could be addressed and improved upon in more sophisticated array structure designs.[63,64]

3. Conclusion

In summary, we have developed a non-volatile OMT device based on the nanosprouts structures of DPh-DNTT organic semiconductor. The optical memory effect is found to be directly

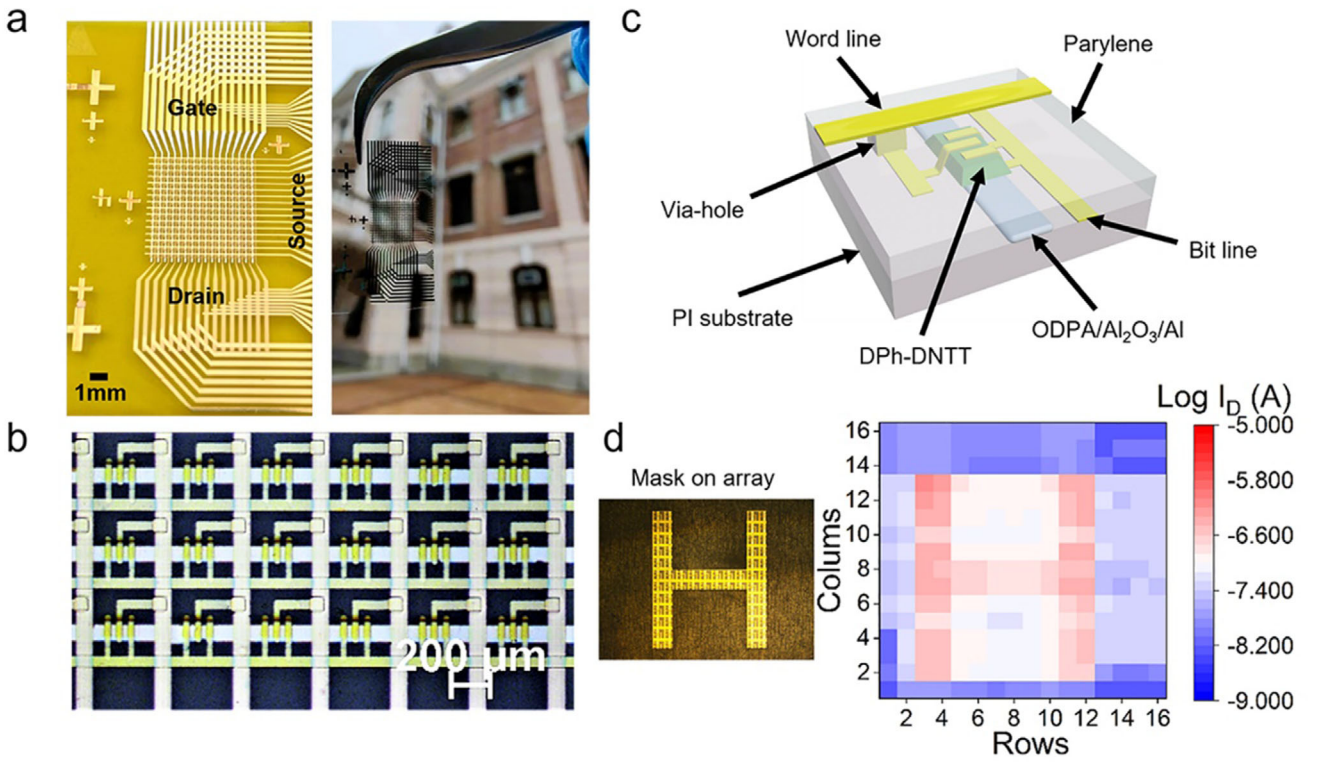

Figure 5. OMT array with image recognition and storage capability. a) Photographs of the 16 × 16 active-matrix OMT array. b) The enlarged view of the pixel area of the OMT array. c) Schematic diagram of an individual memory transistor in the array. d) The demonstration of the image recognition and storage functions of the optical memory transistors array, the current values are read at V_{GS} = 1 V, V_{DS} = 1 V through the homemade automatic test system. The left is the photograph of mask on OMT array, the right is the tested current map after programing (program condition: V_{GS} = 4 V, V_{DS} = 0 V, 445 nm optical power density of 20 mW cm^{-2}, 4s for each gate line).

correlated with the presence of these nanosprouts structures. Utilizing LFM as the primary analytical tool, we have characterized the nanosprouts structures and terrace structures of the DPh-DNTT film as corresponding to the molecular "face on" and "stand up" packing modes, respectively. LFM, utilizing enhanced sensitivity probes, has revealed that the nanosprouts structures present the (110) lattice plane as the exposed surface. Furthermore, employing KPFM and LFM techniques, we have identified the charge trapping sites of this OMT at the interface between the nanosprouts structures and the terrace structures. Finally, we demonstrated an OMT array with image recognition and storage capabilities. Our work highlights the potential of LFM tests for the in-depth understanding of the charge trapping properties of organic materials, which play critical roles in the overall performance of the thin film organic transistors and memories.

4. Experimental Section

Materials: The solvents and SAM (octadecylphosphonic acid (ODPA) 97%) were purchased from Sigma–Aldrich. DPh-DNTT was obtained from Lumtec (99%). Glass was obtained from Epredia. Aluminum and silver were bought from Kurt J.Lesker(99.99%), gold was bought from Hebei Hongju Metal Materials(99.999%). Parylene was purchased from Specialty Coating Systems. Polyimide was obtained from Mitsubishi Chemical Corporation.

Device Fabrication: For the single device OMT fabrication, The glass substrate was sequentially cleaned by ultra-sonicated bath in deionized (DI) water, acetone, isopropanol (IPA) and another acetone for 5 min, and then boiled in IPA bath for 10 min with temperature of 220 °C, and the glass substrate was dried by N_2 flow (99.9%) and then O_2 plasma treatment for 15 min; then 50 nm patterned Al was thermally evaporated onto the glass substrate after the cleaning process, the Al was patterned by shadow mask. The Al layer was employed as the gate electrode of the transistor, the dielectric Al_2O_3 was prepared by anodization process in a sodium citrate electrolyte. The current density during the anodization process was set to the value of 0.7 mA cm^{-2}. The voltage set between the anode (Al) and the cathode (graphite) was 8 V, and the anodization process was completed when the voltage was larger than 8 V. After the fabrication of the Al_2O_3 dielectric layer, the substrate was immersed into 2 mM ODPA in IPA solution for 18 h. The areal capacitance of the ODPA/Al_2O_3 structure was 350 nF·cm^{-2}. Before the DPh-DNTT evaporation, the substrate was ultra-sonicated bath cleaned in IPA for 5 min to remove the ODPA residue, and then dried by the N_2 flow. Then 40 nm DPh-DNTT was thermally evaporated onto the substrate in the base pressure of 1 × 10^{-6} torr at a 0.03 nm s^{-1} deposition rate; in the DPh-DNTT evaporation process, the substrate temperature was controlled by temperature controllers, and the substrate was heat by Peltier heaters. The DPh-DNTT was patterned by a shadow mask. Then 50 nm Ag was thermally evaporated as Source/Drain electrodes, the Ag was patterned by the shadow mask, the W/L was 2000 μm/50 μm.

16 × 16 flexible active matrix OMT array fabrication: 50 nm thick PI film was mounted on glass substrate via Kapton tape, then 150 nm patterned Al was thermally evaporated onto the PI substrate, the Al was patterned by shadow mask. Then Au was thermally evaporated via shadow mask to connect the Al gate lines temporarily. The dielectric Al_2O_3 was prepared by

anodization process, the voltage set between the anode (Al) and the cathode (graphite) was 20 V, and the anodization process was completed when the voltage was larger than 20 V. After the fabrication of the Al_2O_3 dielectric layer, the top part of the PI substrate was cut to separate the gate lines. Then the substrate was immersed into 2 mM ODPA in IPA solution for 18 h. The areal capacitance of the ODPA/Al_2O_3 structure was 248.5 nF·cm^{-2}. Before the DPh-DNTT evaporation, the substrate was ultrasonicated bath cleaned in IPA for 5 min to remove the ODPA residue and then dried by the N_2 flow. Then 40 nm DPh-DNTT was thermally evaporated onto the substrate in the base pressure of 1×10^{-6} torr at a 0.03 nm s^{-1} deposition rate; in the DPh-DNTT evaporation process, the substrate temperature was 100 °C; the DPh-DNTT was patterned by the shadow mask. Then 50 nm Au was thermally evaporated as Source/Drain electrodes, the Au was patterned by the shadow mask, the W/L was 180 µm/30 µm. Then 300 nm parylene was chemical vapor deposited to form the isolation layer, then contact holes were achieved by photoetching plus RIE etching process, the photoresist used was OSCoR 5020 organic compatibility photoresist, the RIE power was 200 W, and the etching time was 7 min; then the photoresist was removed by the OSCoR 5020 stripper, at last, 120 nm Au connect lines were thermally evaporated via shadow mask to connect the devices.

Characterizations: The transfer curves of the optical memory transistors were measured by a Keithley B1500 source-meter in a N_2 filled glovebox. The LED (Luxeon Star) was employed as the light source during the programming process, the optical power density was tuned by tuning the current value of the source meter, and the light intensities were calibrated by a Newport 843-R power meter. The absorption spectra of the DPh-DNTT film were measured by UV–vis absorption spectroscopy (PerkinElmer Lamba 365 UV–vis spectrophotometer). The areal dielectric capacitances were measured by Keysight E4980AL precision LCR meter. The cross-sectional images of organic films were captured by Hitachi S4800 SEM, and the top SEM images were captured by Zeiss Leo 1530 SEM. The LFM test images were captured by an Oxford Cypher AFM with the lateral force mode. The ACF filtering was conducted through Gwyddion software. The KPFM test images were captured by an Oxford Cypher AFM. The XRD results were captured with a Rigaku SmartLab 9 kW X-ray diffractometer with a HyPix-3000 detector, sourced from a copper target. The crystal lattice structures were generated from Diamond software. For the array automatic test system, the DAQ card used was NI USB 6343, the multiplexers used were ADG732 32 channel multiplexers, the current test was conducted by Keithley 2636 source meter.

Supporting Information

Supporting Information is available from the Wiley Online Library or from the author.

Acknowledgements

The work was supported by the InnoHK program of the Innovation and Technology Commission of the Hong Kong SAR Government.

Conflict of Interest

The authors declare no conflict of interest.

Data Availability Statement

The data that support the findings of this study are available from the corresponding author upon reasonable request.

Keywords

lateral force microscopy, optical memory, organic transistor array, structural inhomogeneity

Received: January 28, 2025
Revised: April 25, 2025
Published online:

[1] J. Lee, S. Pak, Y. W. Lee, Y. Cho, J. Hong, P. Giraud, H. S. Shin, S. M. Morris, J. I. Sohn, S. N. Cha, J. M. Kim, *Nat. Commun.* **2017**, *8*, 14734.
[2] S. H. Kim, S. G. Yi, M. U. Park, C. Lee, M. Kim, K. H. Yoo, *ACS Appl. Mater. Interfaces* **2019**, *11*, 25306.
[3] W. Huang, L. Yin, F. Wang, R. Cheng, Z. Wang, M. G. Sendeku, J. Wang, N. Li, Y. Yao, X. Yang, C. Shan, T. Yang, J. He, *Adv. Funct. Mater.* **2019**, *29*, 1902890.
[4] M. D. Tran, H. Kim, J. S. Kim, M. H. Doan, T. K. Chau, Q. A. Vu, J. H. Kim, Y. H. Lee, *Adv. Mater.* **2019**, *31*, 1807075.
[5] F. A. Obrezkov, D. D. Dashitsyrenova, A. G. Lvov, D. Y. Volyniuk, V. Z. Shirinian, P. Stadler, J. V. Grazulevicius, N. S. Sariciftci, S. M. Aldoshin, M. M. Krayushkin, P. A. Troshin, *ACS Appl. Mater. Interfaces* **2020**, *12*, 32987.
[6] T. Leydecker, M. Herder, E. Pavlica, G. Bratina, S. Hecht, E. Orgiu, P. Samorì, *Nat. Nanotechnol.* **2016**, *11*, 769.
[7] S. Z. Hassan, J. Kwon, J. Lee, H. R. Sim, S. An, S. Lee, D. S. Chung, *Adv. Sci.* **2024**, *11*, 2401482.
[8] X. Ren, P. K. L. Chan, *Appl. Phys. Lett.* **2014**, *104*, 113302.
[9] V. Podzorov, M. E. Gershenson, *Phys. Rev. Lett.* **2005**, *95*, 016602.
[10] Q. G. Chen, W. T. Liao, R. Y. Li, I. Sanjuán, N. C. Hsiao, C. T. Ng, T. T. Chang, A. Guerrero, C. C. Chueh, W. Y. Lee, *ACS Mater. Lett.* **2025**, *7*, 682.
[11] F. Shiono, H. Abe, T. Nagase, T. Kobayashi, H. Naito, *Org. Electron.* **2019**, *67*, 109.
[12] T. Xu, S. Guo, W. Qi, S. Li, M. Xu, W. Wang, *ACS Appl. Mater. Interfaces* **2020**, *12*, 21952.
[13] S. Gao, Y. Ren, D. Zhang, X. Wu, Y. Xie, L. Sun, R. Li, F. Yang, W. Hu, *J. Mater. Chem. C* **2024**, *12*, 6943.
[14] S. Lan, J. Zhong, E. Li, Y. Yan, X. Wu, Q. Chen, W. Lin, H. Chen, T. Guo, *ACS Appl. Mater. Interfaces* **2020**, *12*, 31716.
[15] Z. He, H. Shen, D. Ye, L. Xiang, W. Zhao, J. Ding, F. Zhang, C. an Di, D. Zhu, *Nat. Electron.* **2021**, *4*, 522.
[16] S. Duan, X. Zhang, Y. Xi, D. Liu, X. Zhang, C. Li, L. Jiang, L. Li, H. Chen, X. Ren, W. Hu, *Adv. Mater.* **2024**, *36*, 2405030.
[17] C. Lee, K. Pak, J. Choi, M. J. Kim, B. J. Cho, S. G. Im, *Adv. Funct. Mater.* **2020**, *30*, 2004665.
[18] L. Zheng, J. Li, Y. Wang, X. Gao, K. Yuan, X. Yu, X. Ren, X. Zhang, W. Hu, *Nanoscale* **2019**, *11*, 7117.
[19] K. Pei, X. Ren, Z. Zhou, Z. Zhang, X. Ji, P. K. L. Chan, *Adv. Mater.* **2018**, *30*, 1706647.
[20] A. Salleo, R. A. Street, *J. Appl. Phys.* **2003**, *94*, 471.
[21] M. Y. Cho, S. J. Kim, Y. D. Han, D. H. Park, K. H. Kim, D. H. Choi, J. Joo, *Adv. Funct. Mater.* **2008**, *18*, 2905.
[22] Y. Y. Noh, J. Ghim, S. J. Kang, K. J. Baeg, D. Y. Kim, K. Yase, *J. Appl. Phys.* **2006**, *100*, 094501.
[23] L. Zhen, L. Shang, M. Liu, D. Tu, Z. Ji, X. Liu, G. Liu, J. Liu, H. Wang, *Appl. Phys. Lett.* **2008**, *93*, 203302.
[24] Z. Qi, X. Liao, J. Zheng, C. A. Di, X. Gao, J. Wang, *Appl. Phys. Lett.* **2013**, *103*, 053301.
[25] A. Li, X. Wei, Y. He, C. He, M. U. Ali, H. Yang, O. Goto, H. Meng, *Appl. Phys. Lett.* **2018**, *113*, 103301.
[26] C. M. Mate, G. M. McClelland, R. Erlandsson, S. Chiang, *Phys. Rev. Lett.* **1987**, *59*, 1942.
[27] A. J. Weymouth, E. Riegel, B. Simmet, O. Gretz, F. J. Giessibl, *ACS Nano* **2021**, *15*, 3264.
[28] M. Rejhon, F. Lavini, A. Khosravi, M. Shestopalov, J. Kunc, E. Tosatti, E. Riedo, *Nat. Nanotechnol.* **2022**, *17*, 1280.
[29] B. Bhushan, J. N. Israelachvili, U. Landman, *Nature* **1995**, *374*, 607.

[30] A. J. Weymouth, T. Hofmann, F. J. Giessibl, *Science* **2014**, *343*, 1120.
[31] S. Kawai, T. Glatzel, S. Koch, B. Such, A. Baratoff, E. Meyer, *Phys. Rev. B – Condens. Matter Mater. Phys.* **2010**, *81*, 085420.
[32] T. Filleter, J. L. McChesney, A. Bostwick, E. Rotenberg, K. V. Emtsev, T. Seyller, K. Horn, R. Bennewitz, *Phys. Rev. Lett.* **2009**, *102*, 086102.
[33] Y. Naitoh, R. Turanský, J. Brndiar, Y. J. Li, I. Štich, Y. Sugawara, *Nat. Phys.* **2017**, *13*, 663.
[34] R. Pawlak, W. Ouyang, A. E. Filippov, L. Kalikhman-Razvozov, S. Kawai, T. Glatzel, E. Gnecco, A. Baratoff, Q. Zheng, O. Hod, M. Urbakh, E. Meyer, *ACS Nano* **2016**, *10*, 713.
[35] D. Zou, Z. He, M. Chen, L. Yan, Y. Guo, G. Gao, C. Li, Y. Piao, X. Cheng, P. K. L. Chan, *Adv. Mater.* **2023**, *35*, 2211600.
[36] Y. Guo, K. Li, D. Zou, Y. Li, L. Yan, Z. He, T. Zou, B. Huang, P. K. L. Chan, *Adv. Electron. Mater.* **2024**, *10*, 2300570.
[37] T. Wang, K. Zhao, P. Wang, W. Shen, H. Gao, Z. Qin, Y. Wang, C. Li, H. Deng, C. Hu, L. Jiang, H. Dong, Z. Wei, L. Li, W. Hu, *Adv. Mater.* **2022**, *34*, 2105665.
[38] S. Sun, J. Zhu, Z. Wang, Y. Huang, Y. Hu, X. Chen, Y. Sun, L. Li, W. Hu, *Adv. Mater.* **2023**, *35*, 2306975.
[39] X. Tian, J. Yao, S. Guo, Z. Wang, Y. Xiao, H. Zhang, Y. Feng, W. Feng, J. Jie, F. Yang, R. Li, W. Hu, *J. Mater. Chem. C* **2022**, *10*, 2575.
[40] Y. Zhang, Z. Luo, F. Hu, H. Nan, X. Wang, Z. Ni, J. Xu, Y. Shi, X. Wang, *Nano Res.* **2017**, *10*, 1336.
[41] X. Z. Liu, Z. Ye, Y. Dong, P. Egberts, R. W. Carpick, A. Martini, *Phys. Rev. Lett.* **2015**, *114*, 146102.
[42] H. Hölscher, U. Schwarz, O. Zwörner, R. Wiesendanger, *Phys. Rev. B – Condens. Matter Mater. Phys.* **1998**, *57*, 2477.
[43] S. N. Medyanik, W. K. Liu, I. H. Sung, R. W. Carpick, *Phys. Rev. Lett.* **2006**, *97*, 136106.
[44] N. Sasaki, K. Kobayashi, M. Tsukada, *Phys. Rev. B – Condens. Matter Mater. Phys.* **1996**, *54*, 2138.
[45] H. Hölscher, D. Ebeling, U. D. Schwarz, *Phys. Rev. Lett.* **2008**, *101*, 246105.
[46] A. Socoliuc, R. Bennewitz, E. Gnecco, E. Meyer, *Phys. Rev. Lett.* **2004**, *92*, 134301.
[47] P. Steiner, E. Gnecco, F. Krok, J. Budzioch, L. Walczak, J. Konior, M. Szymonski, E. Meyer, *Phys. Rev. Lett.* **2011**, *106*, 186104.
[48] M. J. Kang, E. Miyazaki, I. Osaka, K. Takimiya, A. Nakao, *ACS Appl. Mater. Interfaces* **2013**, *5*, 2331.
[49] M. Munz, *J. Phys. D. Appl. Phys.* **2010**, *43*, 063001.
[50] Y. Yang, K. Xu, L. N. Holtzman, K. Yang, K. Watanabe, T. Taniguchi, J. Hone, K. Barmak, M. R. Rosenberger, *ACS Nano* **2024**, *18*, 6887.
[51] R. Li, X. Zhang, H. Dong, Q. Li, Z. Shuai, W. Hu, *Adv. Mater.* **2016**, *28*, 1697.
[52] Y. Gan, *Surf. Sci. Rep.* **2009**, *64*, 99.
[53] D. S. Wastl, A. J. Weymouth, F. J. Giessibl, *Phys. Rev. B – Condens. Matter Mater. Phys.* **2013**, *87*, 245415.
[54] Z. Zhou, Q. Wu, R. Cheng, H. Zhang, S. Wang, M. Chen, M. Xie, P. K. L. Chan, M. Grätzel, S. P. Feng, *Adv. Funct. Mater.* **2021**, *31*, 2011270.
[55] K. Bagchi, A. Gujral, M. Toney, M. Ediger, *Soft Matter* **2019**, *15*, 7590.
[56] Y. Cang, Z. Wang, C. Bishop, L. Yu, M. Ediger, G. Fytas, *Adv. Funct. Mater.* **2020**, *30*, 2001481.
[57] S. Wang, C. Leung, P. K. L. Chan, *Org. Electron.* **2010**, *11*, 990.
[58] S. M. Wang, C. W. Leung, P. K. L. Chan, *Appl. Phys. Lett.* **2010**, *97*, 023511.
[59] H. F. Haneef, A. M. Zeidell, O. D. Jurchescu, *J. Mater. Chem. C* **2020**, *8*, 759.
[60] M. Tello, M. Chiesa, C. M. Duffy, H. Sirringhaus, *Adv. Funct. Mater.* **2008**, *18*, 3907.
[61] T. He, Y. Wu, G. D'Avino, E. Schmidt, M. Stolte, J. Cornil, D. Beljonne, P. P. Ruden, F. Würthner, C. D. Frisbie, *Nat. Commun.* **2018**, *9*, 2141.
[62] J. Yao, X. Tian, B. Li, Z. Wang, X. Zhang, J. Jie, F. Yang, R. Li, W. Hu, *Adv. Electron. Mater.* **2023**, *9*, 2201027.
[63] V. Correia, J. Oliveira, N. Perinka, P. Costa, E. Sowade, K. Y. Mitra, R. R. Baumann, S. Lanceros-Mendez, *ACS Appl. Electron. Mater.* **2020**, *2*, 1470.
[64] S. Nau, C. Wolf, S. Sax, E. J. W. List-Kratochvil, *Adv. Mater.* **2015**, *27*, 1048.